










Observations of a GX 301–2 Apastron Flare with the *X-Calibur* Hard X-Ray Polarimeter Supported by *NICER*, the *Swift* XRT and BAT, and *Fermi* GBM

Q. Abarr¹, M. Baring², B. Beheshtipour³ , M. Beilicke⁴, G. de Geronimo⁵, P. Dowkontt¹, M. Errando¹, V. Guarino⁶, N. Iyer^{7,8} , F. Kislak⁹, M. Kiss^{7,8} , T. Kitaguchi¹⁰, H. Krawczynski¹ , J. Lanzani¹¹, S. Li¹², L. Lisalda¹, T. Okajima¹³, M. Pearce^{7,8} , L. Press¹, B. Rauch¹, D. Stuchlik¹¹, H. Takahashi¹⁴, J. Tang¹, N. Uchida¹⁴, A. West¹, P. Jenke¹⁵, H. Krimm¹⁶, A. Lien^{17,18}, C. Malacaria^{19,20} , J. M. Miller²¹, and C. Wilson-Hodge¹⁹ 

¹ Washington University in St. Louis, 1 Brookings Dr., CB 1105, St. Louis, MO 63130, USA; errando@wustl.edu, krawcz@wustl.edu

² Rice University, Department of Physics & Astronomy Department, 6100 Main St., Houston TX 77251-1892, USA

³ Max Planck Institute for Gravitational Physics (Albert Einstein Institute), Leibniz Universität Hannover, formerly: Washington University in St. Louis, 1 Brookings Dr., CB 1105, St. Louis, MO 63130, USA

⁴ Former affiliation: Washington University in St. Louis, 1 Brookings Dr., CB 1105, St. Louis, MO 63130, USA

⁵ DG Circuits, 30 Pine Rd., Syosset, NY 11791, USA

⁶ Guarino Engineering, 1134 S Scoville Ave., Oak Park, IL 60304, USA

⁷ KTH Royal Institute of Technology, Department of Physics, SE-106 91 Stockholm, Sweden

⁸ The Oskar Klein Centre for Cosmoparticle Physics, AlbaNova University Centre, SE-106 91 Stockholm, Sweden

⁹ University of New Hampshire, Morse Hall, 8 College Rd., Durham, NH 03824, USA; fabian.kislak@unh.edu

¹⁰ RIKEN Nishina Center, 2-1 Hirosawa, Wako, Saitama 351-0198, Japan

¹¹ NASA Wallops Flight Facility, 32400 Fulton St., Wallops Island, VA 23337, USA

¹² Brookhaven National Laboratory, 98 Rochester St., Upton, NY 11973, USA

¹³ NASA's Goddard Space Flight Center, Greenbelt, MD 20771, USA

¹⁴ Hiroshima University, Department of Physical Science, 1-3-1, Kagamiyama, Higashi-Hiroshima, 739-8526, Japan

¹⁵ University of Alabama in Huntsville, Huntsville, AL 35899, USA

¹⁶ National Science Foundation, 2415 Eisenhower Ave., Alexandria, VA 22314, USA

¹⁷ Center for Research and Exploration in Space Science and Technology (CRESST) and NASA Goddard Space Flight Center, Greenbelt, MD 20771, USA

¹⁸ Department of Physics, University of Maryland, Baltimore County, 1000 Hilltop Circle, Baltimore, MD 21250, USA

¹⁹ ST12 Astrophysics Branch, NASA Marshall Space Flight Center, Huntsville, AL 35812, USA

²⁰ Universities Space Research Association, NSSTC, Huntsville, AL 35805, USA

²¹ University of Michigan, Department of Astronomy, 1085 S. University, Ann Arbor, MI 48109, USA

Received 2019 September 4; revised 2019 December 12; accepted 2019 December 26; published 2020 March 4

Abstract

The accretion-powered X-ray pulsar GX 301–2 was observed with the balloon-borne *X-Calibur* hard X-ray polarimeter during late 2018 December, with contiguous observations by the *Neutron star Interior Composition Explorer Mission (NICER)* X-ray telescope, the *Swift* X-ray Telescope and Burst Alert Telescope, and the *Fermi* Gamma-ray Burst Monitor spanning several months. The observations detected the pulsar in a rare apastron flaring state coinciding with a significant spin up of the pulsar discovered with the *Fermi* Gamma-ray Burst Monitor. The *X-Calibur*, *NICER*, and *Swift* observations reveal a pulse profile strongly dominated by one main peak, and the *NICER* and *Swift* data show strong variation of the profile from pulse to pulse. The *X-Calibur* observations constrain for the first time the linear polarization of the 15–35 keV emission from a highly magnetized accreting neutron star, indicating a polarization degree of $(27_{-27}^{+38})\%$ (90% confidence limit) averaged over all pulse phases. We discuss the spin up and the X-ray spectral and polarimetric results in the context of theoretical predictions. We conclude with a discussion of the scientific potential of future observations of highly magnetized neutron stars with the more sensitive follow-up mission *XL-Calibur*.

Unified Astronomy Thesaurus concepts: Neutron stars (1108); X-ray astronomy (1810); Spectropolarimetry (1973); High mass x-ray binary stars (733); Bianchi cosmology (150)

1. Introduction

In this paper, we report on phase-resolved spectro-polarimetric observations of the accretion-powered, highly magnetized X-ray pulsar GX 301–2 with the *X-Calibur* balloon-borne mission (see Figure 1; Krawczynski et al. 2011; Guo et al. 2013; Beilicke et al. 2014, 2015; Kislak et al. 2017, 2018) in late 2018 December. The observations were accompanied by spectro-temporal observations in overlapping and adjacent periods by the *Neil Gehrels Swift Observatory (Swift)* Burst Alert Telescope (BAT; Barthelmy et al. 2005), the *Swift* X-ray Telescope (XRT; Burrows et al. 2007), the *Neutron star Interior Composition Explorer Mission (NICER)* X-ray telescope (Gendreau et al. 2012), and the *Fermi* Gamma-ray Burst Monitor (GBM; Meegan et al. 2009). The observations covered a particularly interesting epoch in which the pulsar

exhibited rare flaring activity associated with a substantial pulsar spin up.

The pulsar is in an orbit of period ~ 41.5 days and eccentricity 0.462 about the star Wray 977, also known as BP Crucis (Koh et al. 1997; Sato et al. 1986; Doroshenko et al. 2010), an extremely bright B1 Ia hypergiant at a distance of $4.0_{-0.5}^{+0.6}$ kpc (Gaia Collaboration 2018). Wray 977 has an estimated mass of ~ 39 – $63 M_{\odot}$, a radius of $\sim 60 R_{\odot}$, ~ 0.3 au, and shines with a bolometric luminosity of $\sim 5 \times 10^5 L_{\odot}$ (Kaper et al. 2006; Clark et al. 2012). The pulsar has a spin period of ~ 680 s (White et al. 1976) and a 2–10 keV luminosity of 10^{37} – 10^{38} erg s^{−1} (Liu et al. 2018). The pulsar displays bright flares prior to periastron at an orbital phase of ~ 0.93 (Leahy & Kostka 2008). Although GX 301–2 is in a tight orbit with a hypergiant star (its semimajor axis

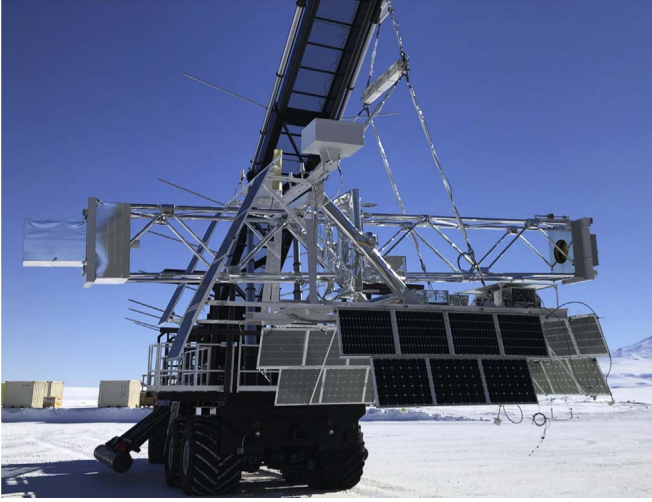


Figure 1. *X-Calibur* hard X-ray polarimeter during integration in McMurdo (Antarctica) in 2018 December. The *InFOCUS* X-ray mirror is used to focus the X-rays onto a scattering polarimeter at the front (right) and back (left) ends of the 8 m long telescope.

is $\sim 19\text{--}30$ au), the X-ray light curves do not show any evidence for eclipses. Parkes et al. (1980), Kaper et al. (2006), and Leahy & Kostka (2008) estimate the inclination (angle between the binary angular momentum vector and the observer) to lie between 44° and 78° .

GX 301–2 is believed to accrete from the wind of its companion, and possibly from a plasma stream (Leahy & Kostka 2008) or a temporary accretion disk (Koh et al. 1997; Nabizadeh et al. 2019). As the material sinks toward the neutron star, it latches onto the magnetic field lines at the magnetospheric radius $r_m \sim 2000\text{--}3000$ km from the center of the neutron star (Lipunov 1992; Mészáros 1992, and references therein). Transferring its angular momentum to the neutron star, the plasma moves along the magnetic field lines until it dissipates its kinetic energy either in a radiative shock above the neutron star surface or in a hydrodynamic shock right at the neutron star surface (Basko & Sunyaev 1975, 1976; Becker et al. 2012; Mushtukov et al. 2015a). The X-ray emission is believed to form through the Comptonization of blackbody, bremsstrahlung, and cyclotron seed photons emitted in and nearby the shocked plasma leading to a power law at low energies with an exponential cutoff in the 10–20 keV energy range (Becker & Wolff 2012; Farinelli et al. 2012; Postnov et al. 2015; West et al. 2017; Wolff et al. 2019).

The literature on accreting X-ray pulsars distinguishes between two idealized radiation patterns associated with the different locales for the energy dissipation, as illustrated in Figure 2. The dissipation in a radiative shock further up in the accretion column is believed to lead to a fan-shaped radiation pattern with most photons leaving the accretion column perpendicular to the flow direction (Davidson 1973). Emission associated with a hydrodynamic shock close to the neutron star surface is expected to lead to a more narrowly focused emission pattern resembling a pencil beam (Burnard et al. 1991; Nelson et al. 1993). Discriminating between these two scenarios is a prime goal of studies of X-ray binaries (XRBs), and X-ray polarimetry stands to play a decisive role.

GX 301–2 observations with *NuSTAR* revealed two cyclotron resonant scattering features (CRSFs) with line centroids E_{CRSF} and Gaussian widths σ_{CRSF} of $(E_{\text{CRSF}}, \sigma_{\text{CRSF}}) = (37 \text{ keV}, 5 \text{ keV})$

and $(50 \text{ keV}, 8 \text{ keV})$ (Fürst et al. 2018; Nabizadeh et al. 2019). The CRSF energies and widths depend on time and on the pulsar phase (Kreykenbohm et al. 2004; Fürst et al. 2018; Nabizadeh et al. 2019). In XRBs, CRSFs are associated with electrons transitioning between quantized Landau levels, the transverse energy discretization relative to the magnetic field direction that emerges from the Dirac equation in quantum electrodynamics (QED). The observation of an electron CRSF at energy E_{CRSF} constrains the magnetic field to be:

$$B \approx \frac{(1+z)}{n} \frac{E_{\text{CRSF}}}{11.57 \text{ keV}} 10^{12} \text{ G}. \quad (1)$$

Here, the positive integer n is the harmonic number of the cyclotron transition. This relation applies to line features at energies significantly lower than $m_e c^2$, i.e., when B is much smaller than the quantum critical field $B_{\text{cr}} = \frac{m_e^2 c^3}{e \hbar} \approx 4.41 \times 10^{13} \text{ G}$, so that the harmonics are evenly spaced.

For a neutron star of mass M and an emission from radius r_{em} (measured from the center of the neutron star), the redshift z is approximately given by:

$$z = \frac{1}{\sqrt{1 - \frac{2GM}{r_{\text{em}} c^2}}} - 1 \approx 0.15 \frac{M}{M_\odot} \left(\frac{r_{\text{em}}}{10 \text{ km}} \right)^{-1}. \quad (2)$$

If the absorption features are interpreted as coming from one region, then the natural $n = 3, 4$ inference would yield $B = 1.1 \times 10^{12} (1+z)$ Gauss, while an $n = 2, 3$ choice gives $B \sim 1.5 \times 10^{12} (1+z)$ Gauss. In such a case, the absence of a prominent $n = 1$ fundamental at lower energies poses an issue. Thus, Fürst et al. (2018) interpret the two features as being fundamentals from distinct regions, in which case they possess higher fields, namely $\sim 3 \times 10^{12} \text{ G}$ and $\sim 4.3 \times 10^{12} \text{ G}$ (for $z = 0$), corresponding to cyclotron absorption radii differing by only around 12%. These fields are substantially above the values inferred from accretion torque models (see Table 1 of Staubert et al. 2019), the converse of what is usually obtained when comparing these two field estimates for X-ray binary pulsars. Some CRSFs are observed to depend on pulse phase, time, and luminosity (Staubert et al. 2019, and references therein). These variations are sometimes attributed to a movement of the radiative shock along the accretion column, or by changes in the magnetic field geometry (e.g., Becker et al. 2012; Mushtukov et al. 2015b).

The polarimetric capability of *X-Calibur* opens up a new degree of freedom in diagnosing the physical environment of GX 301–2. Observations of the linear polarization fraction and angle can provide qualitatively new information on the origin of X-rays in the accretion column or at its impact locale on the neutron star surface, on their birefringent propagation in the magnetosphere, and on the photon interaction cross sections.

The predictions of the polarization of the X-rays from highly magnetized neutron stars depend strongly on the strong-field QED predictions of the birefringence of the magnetized vacuum (Euler & Kockel 1935; Heisenberg & Euler 1936; Weisskopf 1936; Schwinger 1951; Toll 1952; Gnedin & Pavlov 1974; Chan et al. 1979; Heyl & Shaviv 2000) and the mode dependence of the scattering cross sections and absorption coefficients (e.g., Adler et al. 1970; Adler 1971; Canuto et al. 1971; Mészáros & Ventura 1978; Ventura 1979; Arons et al. 1987; Mészáros 1992; Harding & Lai 2006).

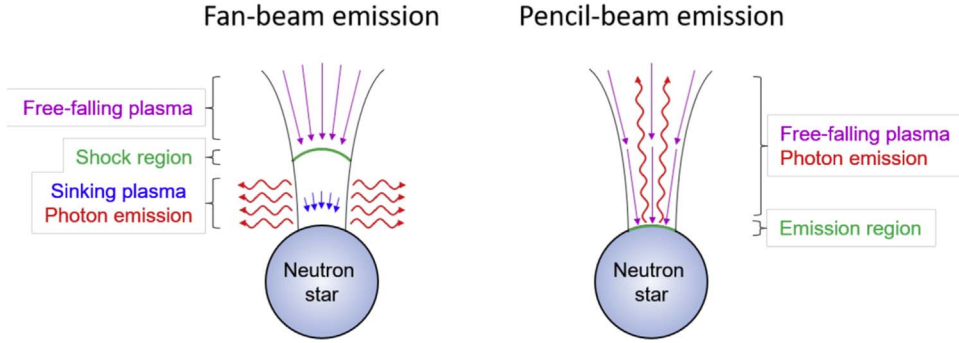


Figure 2. Schematic views of the fan-beam (left) and pencil-beam (right) emission geometries. (Adapted from Schönherr et al. 2007.)

Kii et al. (1986), Kii (1987), and Mészáros et al. (1988) used polarization-dependent radiation transfer calculations to predict the polarization fractions of accreting X-ray pulsars. They found that the mode-dependent scattering cross sections lead to high polarization fractions in certain pulse intervals. Mészáros et al. (1988) determined that the models robustly predict that the phase-resolved flux and polarization fraction should be correlated (anti-correlated) in the fan-beam (pencil-beam) models. The detection of such a correlation can therefore discriminate between the fan-beam and pencil-beam models. This is a design driver for an upgraded version of *X-Calibur*, as described in Section 6.

The rest of the paper is structured as follows. The *X-Calibur* mission and experiment are described in Section 2. The *X-Calibur*, *NICER*, *Swift*, and *Fermi* observations, and data analysis methods are described in Sections 3 and 4, respectively. We present the results of the observations in Section 5 and conclude with a summary and an outlook for the scientific potential of follow-up flights in Section 6. The appendices include a description of the *X-Calibur* Stokes parameter analysis (Appendix A), our estimates of the systematic errors on the *X-Calibur* polarization parameters (Appendix B), and a summary of the spectral results (Appendix C).

All errors and uncertainties are quoted at 1σ -level (68.27% confidence level), unless noted otherwise.

2. The *X-Calibur* Experiment

X-Calibur combines an 8 m long X-ray telescope with arcseconds pointing and a scattering polarimeter (Figure 1). The telescope uses an aluminum-carbon fiber optical bench (Kislat et al. 2017), which is pointed with the Wallops Arc Second Pointer with a pointing stability of $\sim 1''$ root mean square (rms) and a pointing knowledge of $< 15''$ (3σ) (Stuchlik 2015). *X-Calibur*'s energy range is limited to > 15 keV by the absorption in the residual atmosphere at a float altitude of 125,000 feet, and to < 60 keV by the mirror reflectivity. The mirror achieves an angular resolution of 2.5 half-power diameter and effective areas of 93 cm² at 20 keV and 46 cm² at 35 keV (Okajima et al. 2002; Berendse et al. 2003; Tueller et al. 2005; Ogasaka et al. 2008). Grazing incidence mirrors reduce the polarization of cosmic X-ray signals by less than 1% of the true polarization owing to the shallow scattering angles (Sanchez Almeida & Martinez Pillet 1993; Katsuta et al. 2009). The polarimeter is shown in Figure 3 and is made of a Be scattering element inside an assembly of Cadmium Zinc Telluride (CZT) detectors (each 2 mm thick, 2×2 cm² footprint, 64 pixels). Photons preferentially scatter perpendicular to the angle of the electric field of

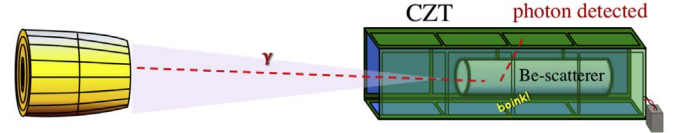


Figure 3. *X-Calibur* detection principle: the X-ray mirror focuses photons onto a Be scattering element. The scattered photon is detected in the surrounding assembly of CZT detectors. The distribution of the azimuthal scattering angles depends on the linear polarization fraction and angle. A rear CZT detector behind the scattering element (at the right side of the detector assembly) is used to monitor the position of the source in the field of view.

the beam with an azimuthal scattering angle distribution of:

$$\frac{dN}{d\psi} \propto \frac{1}{2\pi} [1 + \mu p_0 \cos(2(\psi - \psi_0 - \pi/2))], \quad (3)$$

with p_0 and ψ_0 being the true polarization fraction and angle, ψ the measured azimuthal scattering angle, and $\mu = 51.3\%$ is *X-Calibur*'s modulation factor. A rear CZT detector is positioned behind the scattering slab for monitoring the source location in the field of view. The timing resolution is ~ 1 μ s. The energy resolution increases from ~ 3 keV FWHM at 15 keV to 5 keV FWHM at 35 keV. The detector assembly is shielded by a fully active CsI(Na) shield, and the polarimeter/shield assembly rotates at 1 rpm around the optical axis to minimize systematic errors. Detailed descriptions of the polarimeter and the in-flight performance of all components are given in Beilicke et al. (2014), Kislat et al. (2018), and Q. Abarr et al. (2020a, in preparation).

3. Observations

X-Calibur was launched at 20:45 on 2018 December 29 (all times and dates are UTC) and reached a float altitude of 39.6 km (130,000 feet) roughly 3 hr later. Following the checkout of the pointing system and the in-flight optimization of the anti-coincidence shield settings, *X-Calibur* observed the accreting X-ray pulsars GX 301–2 and Vela X-1 until the flight was aborted owing to a He leak of the balloon at 20:00 on 2019 January 1. The starting times and durations of the *X-Calibur* on-source observation windows are listed in Table 1. The high-balloon-altitude GX 301–2 data set comprises a total of 8.0 hr ON-source and 7.8 hr OFF-source (aiming 1° away from the source).

The *NICER* X-ray Timing Instrument (Gendreau et al. 2016) observed GX 301–2 for 2.0 ks on 2018 December 28 and for

Table 1
Summary of *X-Calibur*, *NICER*, and *Swift* XRT Observations

Instrument	Label	ObsID	Start [MJD]	Exposure [s]
<i>X-Calibur</i>	X-I	1	58482.158310	1080
<i>X-Calibur</i>	X-II	2	58482.168337	653
<i>X-Calibur</i>	X-III	3	58482.188979	925
<i>X-Calibur</i>	X-IV	4	58482.211214	923
<i>X-Calibur</i>	X-V	5	58482.233435	925
<i>X-Calibur</i>	X-VI	6	58482.255660	925
<i>X-Calibur</i>	X-VII	7	58482.277879	925
<i>X-Calibur</i>	X-VIII	8	58482.300110	924
<i>X-Calibur</i>	X-IX	9	58482.322312	928
<i>X-Calibur</i>	X-X	10	58482.344555	924
<i>X-Calibur</i>	X-XI	11	58482.366783	925
<i>X-Calibur</i>	X-XII	12	58482.389004	924
<i>X-Calibur</i>	X-XIII	13	58482.411225	925
<i>X-Calibur</i>	X-XIV	14	58482.433447	916
<i>X-Calibur</i>	X-XV	15	58482.455664	926
<i>X-Calibur</i>	X-XVI	16	58482.477913	923
<i>X-Calibur</i>	X-XVII	17	58482.500132	923
<i>X-Calibur</i>	X-XVIII	18	58482.522364	922
<i>X-Calibur</i>	X-XIX	19	58482.544571	926
<i>X-Calibur</i>	X-XX	20	58482.566831	918
<i>X-Calibur</i>	X-XXI	21	58482.589033	928
<i>X-Calibur</i>	X-XXII	22	58483.117441	219
<i>X-Calibur</i>	X-XXIII	23	58483.135091	757
<i>X-Calibur</i>	X-XXIV	24	58483.151973	986
<i>X-Calibur</i>	X-XXV	25	58483.174523	931
<i>X-Calibur</i>	X-XXVI	26	58483.193260	328
<i>X-Calibur</i>	X-XXVII	27	58483.218975	932
<i>X-Calibur</i>	X-XXVIII	28	58483.241197	930
<i>X-Calibur</i>	X-XXIX	29	58483.263374	925
<i>X-Calibur</i>	X-XXX	30	58483.285587	925
<i>X-Calibur</i>	X-XXXI	31	58483.307799	925
<i>X-Calibur</i>	X-XXXII	32	58483.330011	925
<i>X-Calibur</i>	X-XXXIII	33	58483.352284	936
<i>X-Calibur</i>	X-XXXIV	34	58483.374538	931
<hr/>				
<i>NICER</i>	N-I	1010220101	58,480.09	400
<i>NICER</i>	N-II	1010220101	58,480.16	230
<i>NICER</i>	N-II	1010220101	58,480.28	310
<i>NICER</i>	N-IV	1010220101	58,480.34	1015
<i>NICER</i>	N-V	1010220102	58,481.26	230
<hr/>				
<i>Swift</i> XRT	S-I	00031256019	58,480.10	1055
<i>Swift</i> XRT	S-II	00031256020	58,481.15	1010
<i>Swift</i> XRT	S-III	00031256021	58,482.73	960
<i>Swift</i> XRT	S-IV	00031256022	58,483.66	960
<i>Swift</i> XRT	S-V	00031256023	58,484.00	760
<i>Swift</i> XRT	S-VI	00031256024	58,485.52	895
<i>Swift</i> XRT	S-VII	00031256025	58,486.39	990
<i>Swift</i> XRT	S-VIII	00031256026	58,487.38	540
<i>Swift</i> XRT	S-IX	00031256027	58,488.51	920

0.2 ks on December 29. Observations on December 28 were split into five shorter observation windows and were analyzed independently. The *Swift* X-Ray Telescope (XRT) observed GX 301–2 from MJD 58,480 through MJD 58,488 in nine individual pointings between 0.5 and 1.1 ks for a total of 8.1 ks. Details about the *NICER* and *Swift* observations are summarized in Appendix C, Table 1. Observing windows are labeled X-I–X-XXXIV for *X-Calibur*, N-I to N-V for *NICER*, and S-I to S-IX for *Swift* XRT. The *Swift* BAT and *Fermi* GBM observe GX 301–2 on a regular basis. We use the following results obtained for individual orbits and results averaged over individual days.

4. Data Analysis

4.1. *X-Calibur* Data Analysis

The *X-Calibur* data analysis uses single-pixel CZT events without shield veto. The energy deposited in the CZT is estimated based on the calibration of the polarimeter with a ^{152}Eu source with low-energy lines at 39.52 keV ($K_{\alpha 2}$), 40.12 keV ($K_{\alpha 1}$), 45.7 keV, and 121.78 keV.

An event consists of the pixel number i (located at position $\mathbf{x}_i = (x, y, z)_i$ in the detector reference frame, with x and y being the coordinates in the focal plane and z pointing toward the source), the energy E deposited in the CZT detectors, and the GPS event time t . Consistent with the exponential cutoff of the energy spectrum (e.g., Fürst et al. 2018), *X-Calibur* does not detect a significant excess of photons with >35 keV energy deposits, and we thus only use $E < 35$ keV events. The events enter the analysis with weights that were optimized based on the detector response as inferred from Monte Carlo simulations (Appendix A). For light curves, we normalize the weights so that the weighted event rate equals the true source rate.

The polarization analysis uses the Stokes parameters I (total flux), Q (the linearly polarized flux along the north–south direction), and U (the linearly polarized flux along the direction rotated 45° counterclockwise from the north–south direction when looking at the source) which are the weighted sums of the corresponding Stokes parameters of individual events (Kislat et al. 2015; Strohmayer 2017). The main results are given in terms of the normalized Stokes parameters:

$$Q = Q/I, \quad (4)$$

$$U = U/I, \quad (5)$$

so that Q (U) equals 1 for a beam 100% linearly polarized along the north–south (northeast–southwest) direction. The reconstructed polarization fraction p_r is given by

$$p_r = \sqrt{Q^2 + U^2}, \quad (6)$$

and the reconstructed polarization angle ψ_r is given by

$$\psi_r = \frac{1}{2} \arctan(U/Q) = \frac{1}{2} \arctan(U/Q). \quad (7)$$

During the observations, we switch every 15 minutes between observations targeting GX 301–2 (ON observations) and observations of four fields each located in a cross-pattern 1° away from the source in pitch and in yaw (OFF observations). As the Stokes parameters are additive, we can infer the Stokes parameters of the source beam by calculating the Stokes parameters for the ON observations and OFF observations, and subtracting the OFF values from the ON values after scaling the OFF values according to the ON and OFF observation time ratio. Details of the Stokes parameter analysis and background subtraction procedure are given in Appendix A. The systematic error on a measured polarization fraction p_r is (Appendix B)

$$\Delta p_r = 7.25\% \times p_r. \quad (8)$$

The error Δp_r is our best estimate of the maximum possible error.

We fit the *X-Calibur* energy spectrum with *XSPEC* (Arnaud 1996; Arnaud et al. 2017) using Response Matrix Files and Auxiliary Response Files derived from Monte Carlo simulations.

Table 2
GX 301–2 Phase Model Parameters Used in this Paper

Parameter	Value
t_0	58477.024509 (MJD)
$\dot{\phi}$	$126.350509 \text{ day}^{-1}$
$\ddot{\phi}$	$0.0769078 \text{ day}^{-2}$
$\ddot{\phi}$	$-0.00868925 \text{ day}^{-3}$
ϕ	$0.001075897 \text{ day}^{-4}$

4.2. NICER, Swift, and Fermi Data Analysis

The *NICER* data were processed using *NICERDAS* v2018–11–19_V005a included in *HEASOFT* v6.25. Data were calibrated, cleaned, and combined using the *nicerl2* script with default screening filters. For spectral analysis, channels corresponding to energies 2–10 keV were selected.

The *Swift* XRT data were taken entirely in a windowed timing mode analyzed with the *CALDB* version 20180710 and with *HEASOFT* v6.25, using *swxwt0to2s6_20131212v015* response function. The absorption models were fit within the *xspec* command.

The *Swift* BAT data analysis uses the *HEASOFT* v6.23 software and *BAT CALDB* version 20171016. The BAT light curves in eight energy bands (14–20, 20–24, 24–35, 35–50, 50–75, 75–100, 100–150, and 150–195 keV) are created from the BAT survey data with the same methodology that was used for the previous BAT survey catalogs (Oh et al. 2018; Baumgartner et al. 2013). The 15–50 keV light curve is from the BAT transient monitor (Krimm et al. 2013).

The *Fermi* GBM results were taken from the National Space, Science, and Technology Center (NSSTC) web page. The results are derived from the GBM NaI detectors binned in 0.256 s time bins and use the 12–25 keV and 25–50 keV energy channels.²² The spin frequencies are extracted using techniques described in Finger et al. (1999) and Jenke et al. (2012).

4.3. Orbital and Pulsar Phases

We compute the orbital phase with the parameters from Doroshenko et al. (2010), with the last recorded periastron passage on MJD $53,531.65 \pm 0.01$, an orbital period of $P = 41.472$ days, and a period derivative of $\dot{P} = (-3.7 \pm 0.5) \times 10^{-6} \text{ s s}^{-1}$.

We calculate the pulsar phase with the following phase model derived from *Fermi* GBM data:

$$\phi(t) = \dot{\phi}(t - t_0) + \frac{\ddot{\phi}}{2}(t - t_0)^2 + \frac{\ddot{\phi}}{6}(t - t_0)^3 + \frac{\ddot{\phi}}{24}(t - t_0)^4, \quad (9)$$

with t being the barycentered time. The model parameters are given in Table 2.

5. Results

5.1. Timing Results

Figure 4 shows the 15–50 keV fluxes measured with the *Swift* BAT. The graph clearly shows the 41.5 day orbital period. The *X-Calibur* observations from MJD 58,482.1521–58,483.3912 (orbital phases 0.37–0.40) fall into a rare period of a flare close

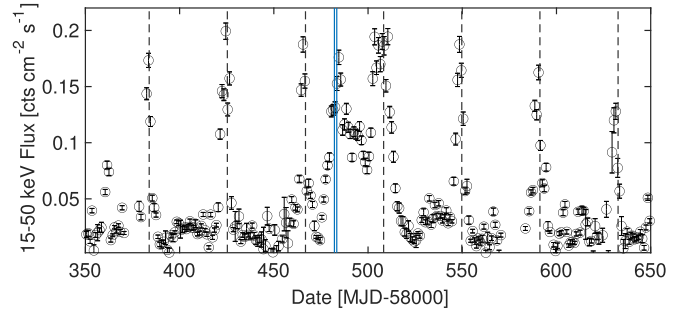


Figure 4. GX 301–2 15–50 keV fluxes measured with the *Swift* BAT instrument (Lien & Krimm 2019). The time interval of the *X-Calibur* observations is marked by the solid blue vertical lines. The periastron passages are marked by the dashed black vertical lines.

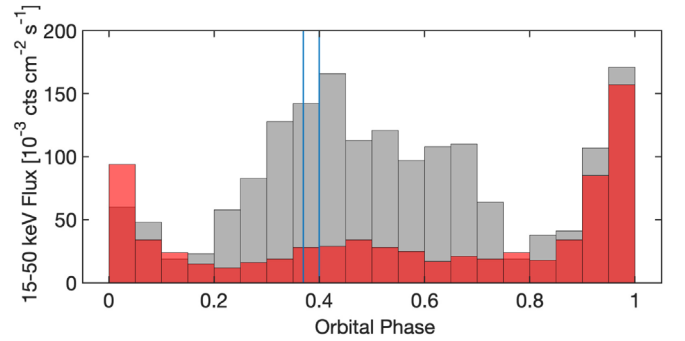


Figure 5. Average GX 301–2 *Swift* BAT 15–50 keV flux in the 11 orbital cycles before the apastron flare (red histogram), and in the orbital cycle of the apastron flare (gray histogram). The time interval of the *X-Calibur* observations is marked by two vertical blue lines.

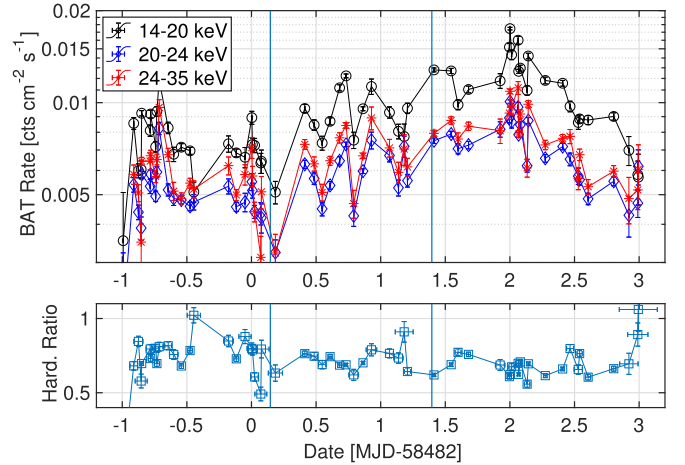


Figure 6. GX 301–2 fluxes measured with the *Swift* BAT instrument in three different energy bands (top panel) and the 24–35 keV to 14–20 keV hardness ratio (bottom panel) during the apastron flare. The time interval of the *X-Calibur* observations is marked by two vertical blue lines.

to apastron. Figure 5 compares the *Swift* BAT 15–50 keV count rate measured during the orbit covering the apastron flare with the average count rates measured during the previous eleven orbits. The activity was enhanced during the orbit of the apastron flare, with a pronounced peak at an orbital phase around 0.4.

The *Swift* BAT data allows us to scrutinize the hard X-ray emission for spectral variability. Figure 6 presents the 14–20 keV, 20–24 keV, and 24–35 keV light curves and the 24–35 keV to 14–20 keV hardness ratios. The rms of the hardness ratios is

²² <https://gammaray.nsstc.nasa.gov/gbm/science/pulsars.html>

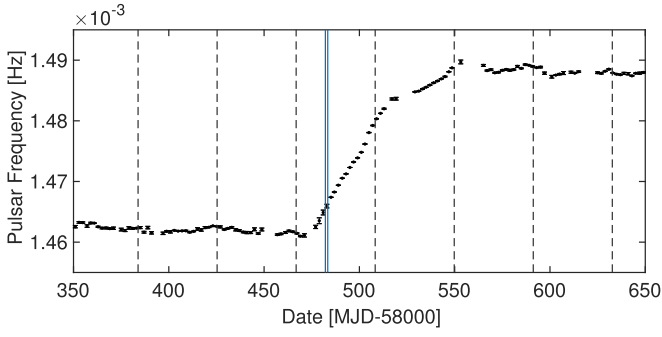


Figure 7. GX 301–2 spin frequency as measured by the *Fermi* GBM from 12 to 50 keV observations between 2018 August 20 and 2019 June 16 (from the NSSTC GBM footnote 22). The time period of the *X-Calibur* observations is shown by two vertical blue solid lines. The periastron passages are marked by vertical dashed lines.

0.103 corresponding to an rms of the photon indices Γ (from $dN/dE \propto E^{-\Gamma}$) of $\Delta\Gamma \approx 1$. We do not discern a clear pattern linking the hardness ratio excursions to the flux level or the flux history except for a pronounced hardening of the energy spectra at the end of the flaring periods at MJD 58,481.5539, MJD 58,483.1819, and MJD 58,484.9899.

The spin frequencies measured with the *Fermi* GBM in the 12–50 keV band (Figure 7) show a spectacular spin up coinciding with the exceptionally bright orbit. During the orbit (41.5 days) covering the *X-Calibur* observations, the spin frequency (period) increased from 1.461 mHz (spin period 684 s) on MJD 58,471.2 to 1.482 mHz (spin period 675 s) on MJD 58,512.9 at a rate of $5.8 \times 10^{-12} \text{ Hz s}^{-1}$ (see also Nabizadeh et al. 2019). The next orbit saw a much slower spin up from 1.482 mHz on MJD 58,512.9 to 1.490 mHz on MJD 58,553.2 at a rate of $2.3 \times 10^{-12} \text{ Hz s}^{-1}$. The spin-up rate is clearly correlated with an enhanced X-ray flux (Figure 8), bolstering the hypothesis that a change of the accretion rate or accretion mode is causing the spin up. Interesting features include the simultaneous dip of the X-ray flux and spin-up rate at MJD 58,492, the decrease of the spin-up rate between MJD 58,502 and MJD 58,510 during a phase of rather constant elevated X-ray flux levels, and the factor two lower spin up during MJD 58,546 and MJD 58,548 when compared to the spin up one orbit earlier (MJD 58,503–MJD 58,510) at similar flux levels.

Koh et al. (1997) and Bildsten et al. (1997) reported similar spin-up phases detected with the BATSE gamma-ray detectors. At the time, the spin frequency increased over 23 days (MJD 48,440–48,463) from 1.463 to 1.473 mHz at a rate of $4.5 \times 10^{-12} \text{ Hz s}^{-1}$ and over 15 days (MJD 49,245–49,230) from 1.474 to 1.478 mHz at a rate of $3.0 \times 10^{-12} \text{ Hz s}^{-1}$. All rapid spin-up periods were accompanied by heightened apastron activity.

Figure 9 shows the GX 301–2 detection in the *X-Calibur* rear CZT detector. The image allows us to verify and refine the X-ray mirror alignment calibration (see also Appendix B). Figure 10 presents the 15–35 keV ON and OFF light curves from the polarimeter section of the detector (without the rear CZT detector). Note that each data point corresponds to one 15 minute run covering slightly more than one pulsar period. *X-Calibur* detected the source with a mean 15–35 keV rate of 0.23 Hz. Figure 11 compares the X-ray light curves from *X-Calibur*, *Swift* BAT, *Swift* XRT, and *NICER* taken around the time of the *X-Calibur* campaign. The flux level increased as

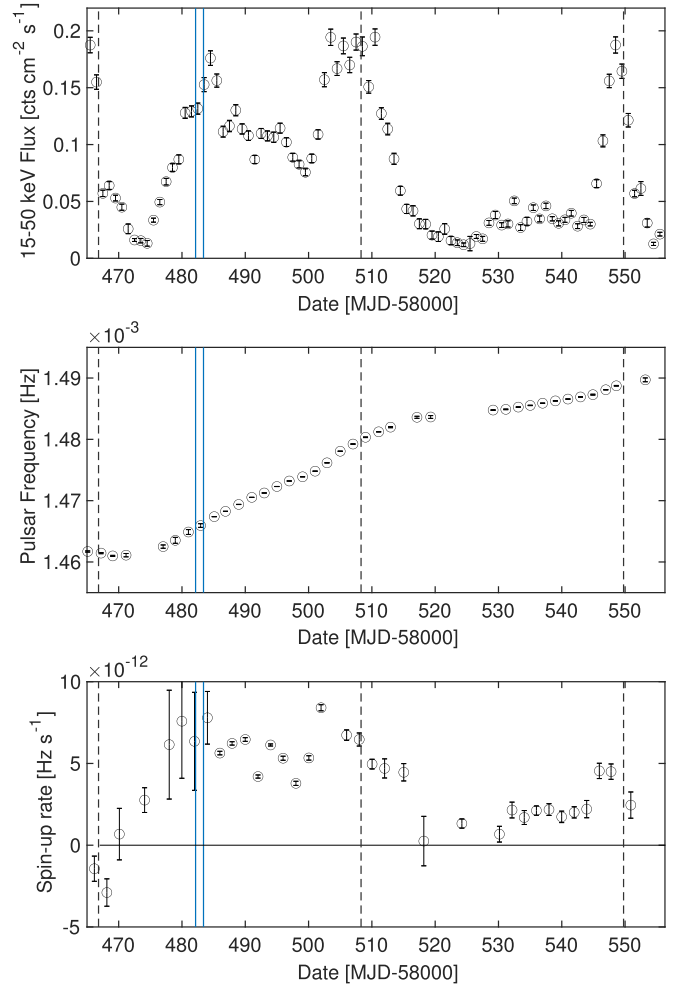


Figure 8. *Swift* BAT GX 301–2 hard X-ray fluxes (upper panel), and GBM spin frequencies (center, from the NSSTC GBM footnote 22) and spin-up rates (bottom) for the two orbits with significant spin up. The time period of the *X-Calibur* observations is shown by two vertical blue lines. The periastron passages are marked by dashed vertical lines.

the observation campaign unfolded and peaked a day after the *X-Calibur* observations ended.

Figure 12 reports the average pulse profiles measured with the *Swift* XRT (0.2–10 keV), *NICER* (0.2–12 keV), and *X-Calibur* (15–35 keV). All three pulse profiles show one peak strongly dominating over the other. The shape of the *X-Calibur* 15–35 keV pulse profile measured during the spin-up epoch deviates significantly from the shapes of the 18–30 keV pulse profiles recorded on 2014 October 29 (orbital phase 0.65), 2015 October 4 (orbital phase 0.85), and 2019 March 3 (orbital phase 0.89) with *NuSTAR*. Whereas the *NuSTAR* pulse profiles show two pulses with approximately equal fluences (flux integrated over time, see Figures 3 and 4 of Nabizadeh et al. 2019), the fluence of the main *X-Calibur* peak (phase 0.8–1.14) exceeds that of the secondary peak 1/2 period later by a factor of ≈ 2 with a statistical significance of more than five standard deviations. The *NICER* (not shown here) and *Swift* data sets have sufficiently high signal-to-noise ratios to reveal significant variations of the pulse profiles from pulse to pulse (Figure 13). Such pulse profile variations can be caused by alterations in the accretion rate and by changes of the accretion and emission geometries.

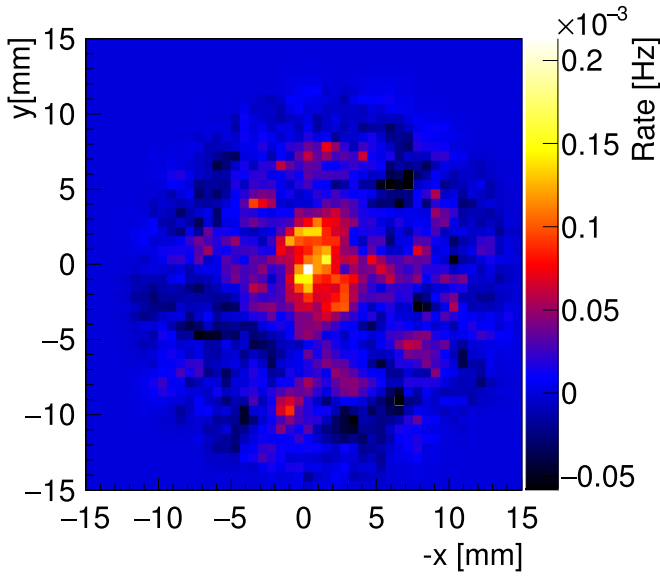


Figure 9. *X-Calibur* focal plane image of the X-ray pulsar GX 301–2 recorded with the rear CZT detector (ON counts minus OFF counts). The image is referenced to the celestial north direction (up). We only used half of the detector for this image, as the readout ASIC of the second half worked only intermittently. This was the only ASIC (out of 34) showing problems during the flight. The spatial extent of the image is dominated by the mirror point-spread function.

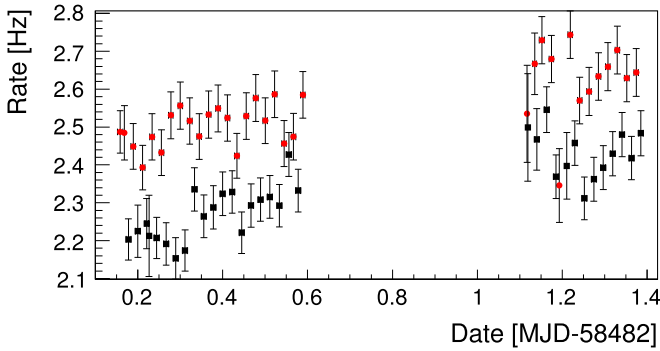


Figure 10. *X-Calibur* 15–35 keV detection rates on-source (red) and off-source (black) revealing an average source count rate of 0.23 Hz. The rates are raw rates in the sense that they have not been corrected for the flight altitude and elevation-dependent atmospheric absorption.

5.2. Spectral Results

The large absorption column observable in the *NICER* and *Swift* energy spectra reduces the count rate dramatically below 2 keV. We select channels with energies between 2 and 10 keV for spectral analysis, and fit them with a power-law continuum going through a partially covered absorber, and an additional Gaussian line

$$N_{\text{H}}^{\text{gal}} \times ((cN_{\text{H},1} + (1 - c)N_{\text{H},2}) \times \text{power law} + \text{Line}), \quad (10)$$

where $N_{\text{H}}^{\text{gal}}$ was fixed to the galactic equivalent column density of $1.7 \times 10^{22} \text{ cm}^{-2}$, reported in (Kalberla et al. 2005).

The results are reported in Tables 3–4. Given the wide variation of the signal-to-noise ratios of the different data sets, some of the energy spectra do not constrain some of the parameters of the model from Equation (10). In those cases, the parameters without errors in Tables 3–4 were fixed to the reported values during the fitting process. For example, in observation *SI* (Figure 14, top,

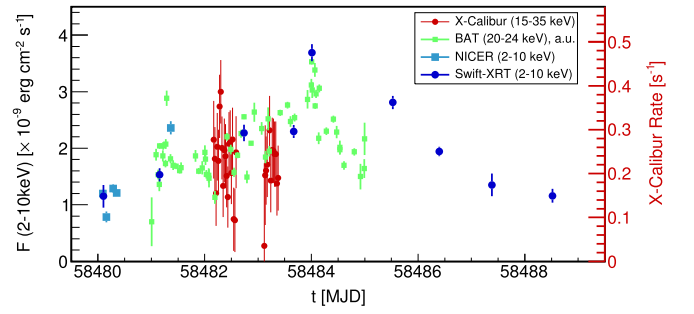


Figure 11. *X-Calibur* (15–35 keV), *Swift* XRT BAT (20–24 keV), *NICER* (2–10 keV), and *Swift* XRT (2–10 keV) GX 301–2 detection rates around the apastron flare.

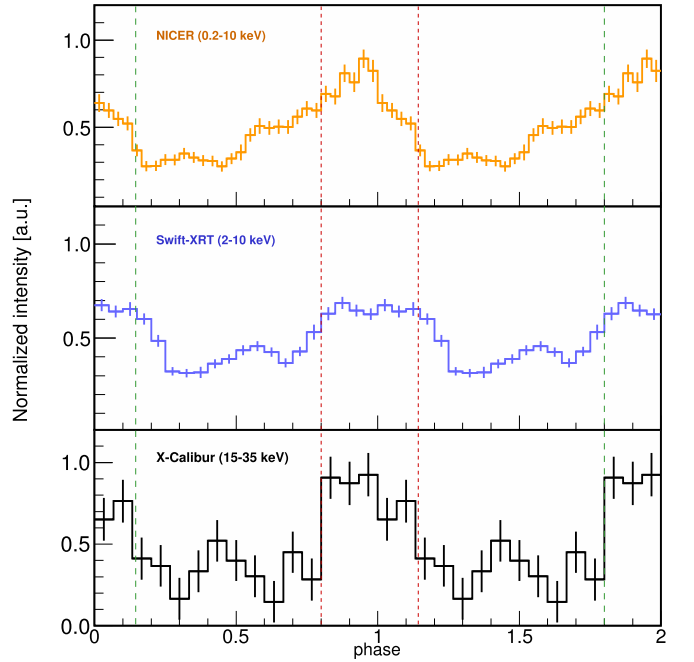


Figure 12. *NICER* (0.2–12 keV), *Swift* XRT (0.2–10 keV), and *X-Calibur* (15–35 keV) time-averaged GX 301–2 pulse profiles. The vertical dashed lines indicate the beginning and end of the main pulse (phase intervals 0.8–1.14).

and Table 4) the data do not allow us to constrain the second absorption component, so we fit the spectrum using Equation (10) with $c = 1.0$ and $N_{\text{H},2} = 0$. For the main absorbing component we find N_{H} values of between $\sim 33 \times 10^{22} \text{ cm}^2$ and $\sim 90 \times 10^{22} \text{ cm}^2$. The N_{H} of the main component decreases through the apastron flare until MJD 58,485.52 (observation *S VI*). Most of our values are higher than the pre-periastron column densities of between $\sim 15 \times 10^{22} \text{ cm}^2$ and $\sim 40 \times 10^{22} \text{ cm}^2$ from Suchy et al. (2012) and Fürst et al. (2018), and lower than the periastron values of between $\sim 115 \times 10^{22} \text{ cm}^2$ and $\sim 175 \times 10^{22} \text{ cm}^2$ of Fürst et al. (2011).

The *NICER* energy spectra show clear Fe $K\alpha$ lines, and some marginally significant deviations of the data from the best-fit model between 2 and 3 keV (Figure 14, top). The *Swift* XRT spectra also show the presence of the Fe $K\alpha$ line (Figure 14, middle) throughout the whole observation period.

The *X-Calibur* 15–35 keV energy spectrum is fitted with a power-law model. We obtain a 15–35 keV flux of $(7.4^{+1.4}_{-1.3}) \times 10^{-9} \text{ erg cm}^{-2} \text{ s}^{-1}$ and a power-law index of 4.2 ± 0.6 (1σ errors). The photon index agrees within statistical errors

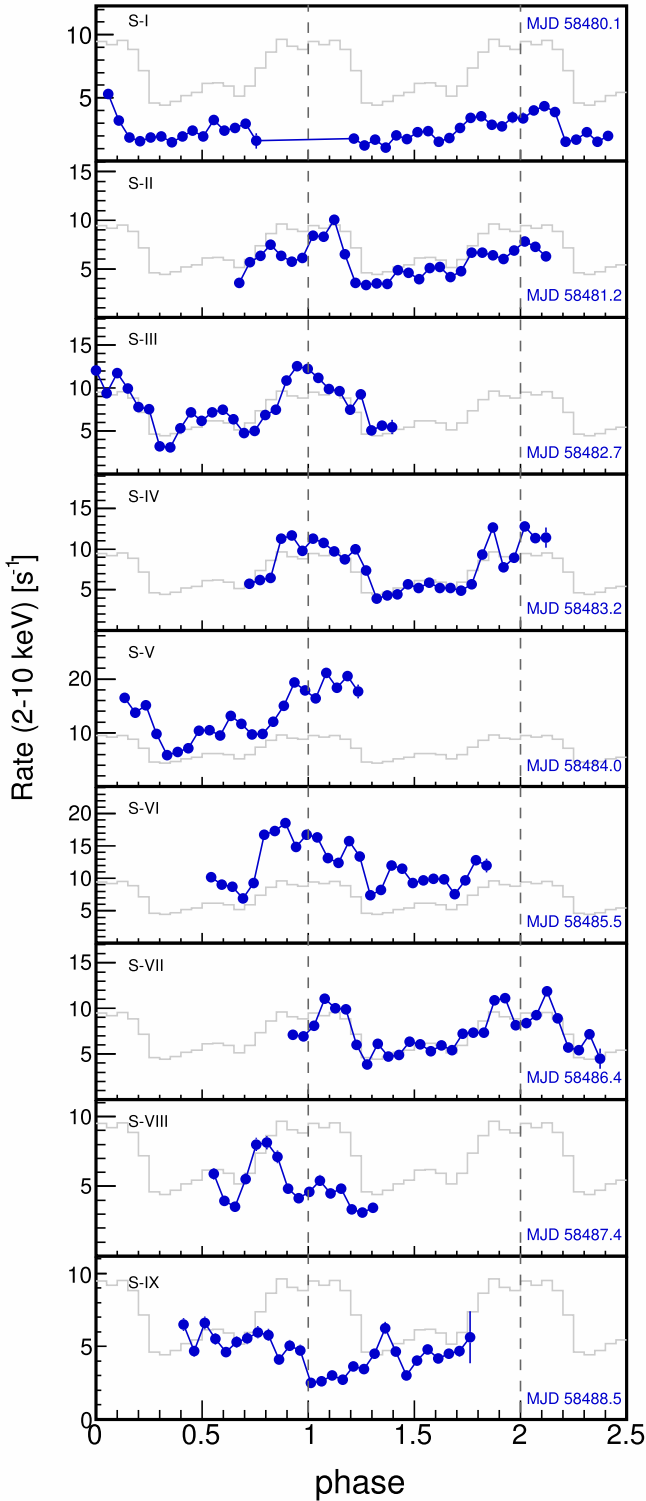


Figure 13. Individual *Swift* XRT (0.2–10 keV) GX 301–2 pulse profiles showing large variations in pulse profiles (note the different scale on vertical axis). The light-curve data is binned in 34 s long time intervals. The average XRT pulse profile is shown in gray for reference. The dashed vertical lines are shown to guide the eye.

with the energy spectrum measured with *NuSTAR* on 2019 March 3, which exhibits a rollover from a photon index of $\Gamma = 2$ at 20 keV to $\Gamma = 4$ at 30 keV (Figure 6 of Nabizadeh et al. 2019).

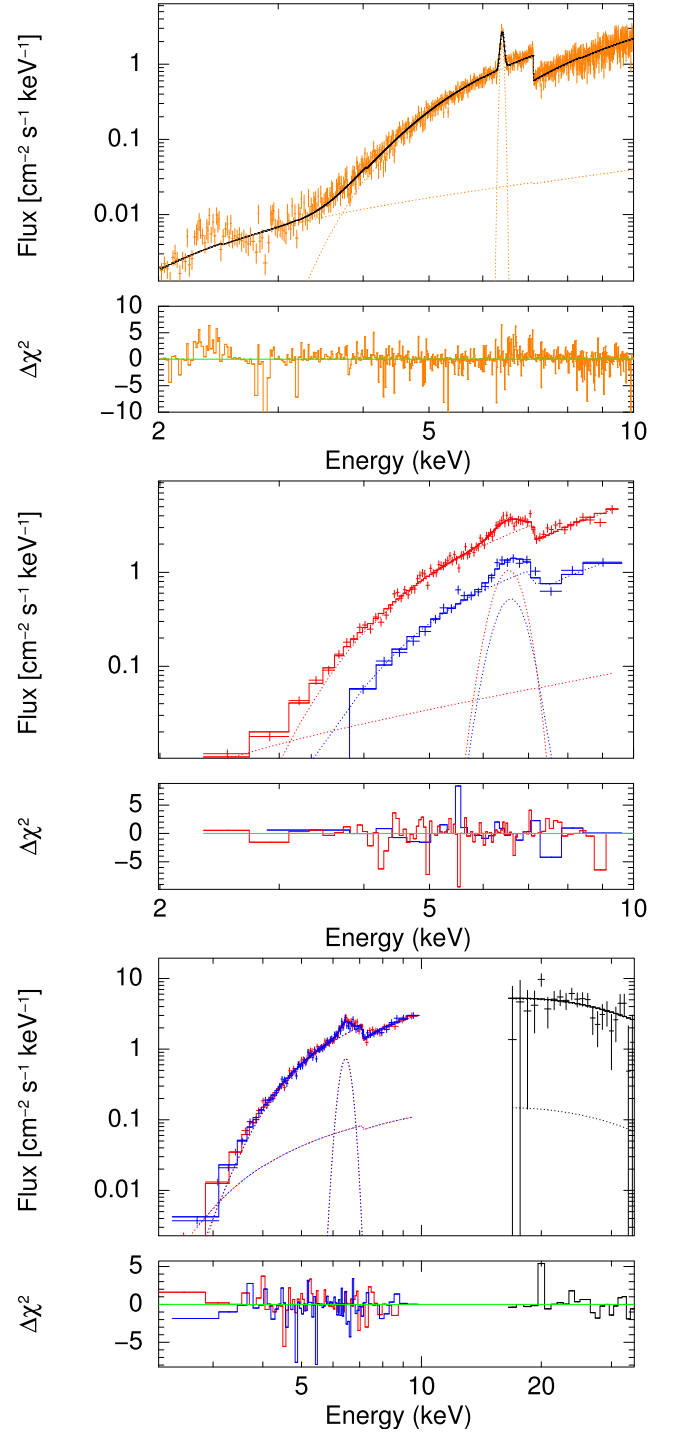


Figure 14. Top: *NICER* GX 301–2 energy spectrum measured on MJD 58,480.34 (observation N-IV from Table 1). Middle: *Swift* XRT spectra from observation S I (in blue) and S V in red (see Tables 1 and 3 for details). Bottom: Joint *Swift* XRT (observations S III and S IV from Table 1) and *X-Calibur* GX 301–2 energy spectrum measured on MJD 58,482 and MJD 58,483. The two top panels also show the best-fit model (solid lines) and the model components (dashed lines) from Equation (10), while the bottom panel displays the model components from Equation (11).

We study the broadband 2–35 keV energy spectrum by simultaneously fitting the *Swift* XRT (observations S III and S IV) and *X-Calibur* data (Figure 14, bottom) with a power-law model with an exponential cutoff, a partially covered absorber,

Table 3
Spectral Results from *NICER* Observations

Observation:	N-I	N-II	N-III	N-IV	N-V
$F_{2-10\text{ keV}} [\times 10^{-9} \text{ erg cm}^{-2} \text{ s}^{-1}]$	1.20 ± 0.06	0.78 ± 0.10	1.29 ± 0.08	1.21 ± 0.02	2.36 ± 0.12
$N_{\text{H},1} [10^{22} \text{ cm}^{-2}]$	78.1 ± 2.4	82.5 ± 4.5	80.3 ± 2.7	86.5 ± 1.8	52.2 ± 2.7
$N_{\text{H},2} [10^{22} \text{ cm}^{-2}]$	2.7 ± 1.0	4.4 ± 1.6	4.5 ± 1.8	2.6 ± 0.6	0.05 ± 0.83
Cov. Frac.	0.992 ± 0.001	0.986 ± 0.003	0.994 ± 0.001	0.990 ± 0.001	0.961 ± 0.005
$\text{PL}_{\text{Norm}} [\text{cm}^{-2} \text{ s}^{-1} \text{ keV}^{-1}]$	0.53 ± 0.10	0.29 ± 0.09	0.60 ± 0.13	0.30 ± 0.04	0.09 ± 0.02
PL_{Γ}	1.21 ± 0.08	1.09 ± 0.14	1.21 ± 0.09	0.85 ± 0.06	0.16 ± 0.09
$\text{Fe K}\alpha \text{ A} [10^{-3} \text{ s}^{-1} \text{ cm}^{-2}]$	3.4 ± 0.3	2.6 ± 0.3	5.3 ± 0.5	4.3 ± 0.2	5.0 ± 0.7
$\text{Fe K}\alpha \text{ E} [\text{keV}]$	6.41 ± 0.01	6.39 ± 0.01	6.40 ± 0.01	6.41 ± 0.01	6.41 ± 0.01
$\text{Fe K}\alpha \sigma [\text{keV}]$	0.02 ± 0.02	0.02	0.060 ± 0.011	0.039 ± 0.007	0.068 ± 0.018
χ^2/NDF	0.97	1.00	0.93	1.14	1.06

Note. The errors are on 1σ confidence level.

and an additional Fe–K α fluorescence line:

$$N_{\text{H}}^{\text{gal}} \times ((cN_{\text{H},1} + (1 - c)N_{\text{H},2}) \times E^{-\Gamma} \exp(-E/E_{\text{fold}}) + \text{Line}). \quad (11)$$

A model with $\Gamma = 0.04 \pm 0.21$, $E_{\text{fold}} = 7.95 \pm 0.78$ keV, and $N_{\text{H},1} = (56 \pm 8) \times 10^{22} \text{ cm}^2$ gives a good fit to the broadband data, with $\chi^2/\text{NDF} = 159.2/155$. The values of the spectral parameters are similar to those obtained by Fürst et al. (2018) using *NuSTAR* observations, with the exception of the softer photon index of $\Gamma \sim 0.8$ obtained by Fürst et al. (2018).

5.3. X-Calibur Polarization Analysis

All polarization results are given in the 15–35 keV band for three data sets (see lower panel in Figure 12): (i) the entire data set, (ii) the main pulse (pulsar phase 0.8–1.14), and for (iii) the bridge and secondary pulse emission (pulsar phase 0.14–0.8). Figure 15 presents the modulation curves (azimuthal scattering angle distributions) for the ON and OFF observations. Neither the ON nor the OFF distributions show obvious modulations.

Figure 16 presents the results in the Q – U plane for all three data sets. The statistical significance for a polarization detection can be calculated with Q and U , which have slightly smaller relative errors than Q and U . The overall results deviate by $\sqrt{(Q/\sigma_Q)^2 + (U/\sigma_U)^2} = 1.41$ (entire emission), 1.47 (main pulse), and 0.78 (bridge and secondary pulse) standard deviations from zero polarization ($Q=0$ and $U=0$). The *X-Calibur* observations thus did not lead to a significant detection of a non-zero polarization.

For the pulse-integrated emission, Figure 17 shows the Q and U parameters for the background-subtracted ON data and the OFF background data as a function of time. It can be seen that the Q and U parameters of the ON and OFF observations are consistent with zero polarization for all time intervals. The same applies to the Q and U parameters of the entire OFF data set.

Figure 18 presents the observational constraints on the polarization fraction p_0 and angle ψ_0 . We use a Bayesian analysis with a flat prior of the polarization fraction p_0 between 0% and 100% and the polarization angle ψ_0 between 0 and π (Quinn 2012; Kislat et al. 2015):

$$dP_0(p_0, \psi_0) = \text{const } dp_0 d\psi_0 \propto 1/\sqrt{Q^2 + U^2} dQ dU. \quad (12)$$

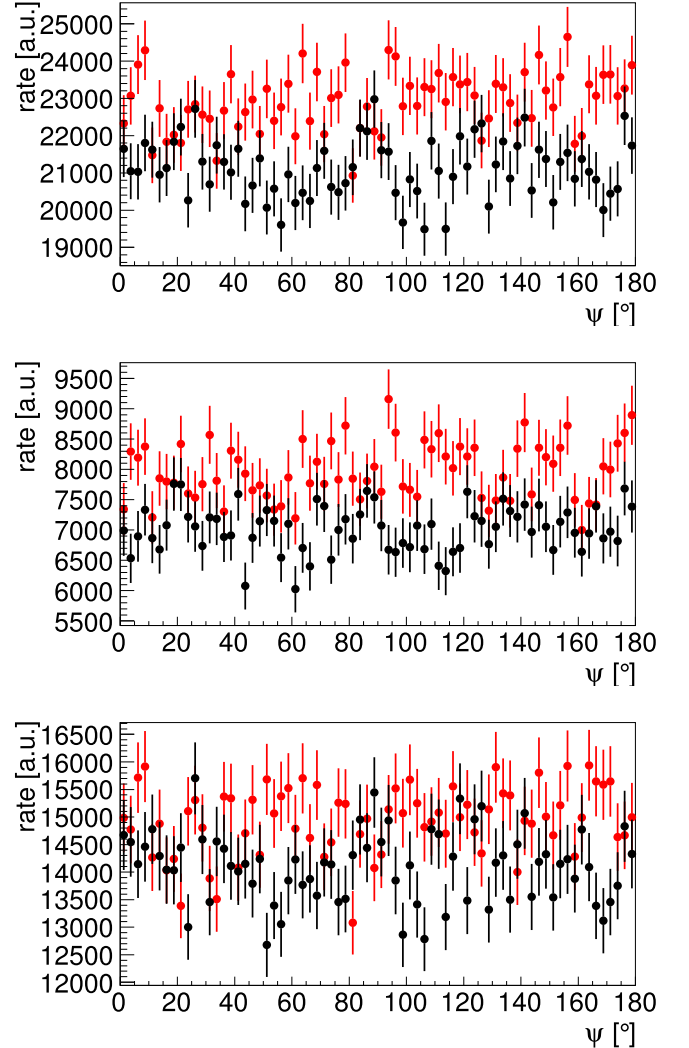


Figure 15. Distribution of the azimuthal scattering angles for the entire emission (top panel), the main pulse (phase 0.8–1.14, center panel), and for the bridge and secondary pulse emission (phase 0.14–0.8, bottom panel) for the ON (red) and OFF (black) data. Individual events enter the analysis with a weight, and we thus give the rate per bin (i.e., the weighted number of events per unit time per bin) in arbitrary units (a.u.).

The most likely true parameter combination p_0 and ψ_0 is shown by a cross mark, and the confidence regions are shown by contours and the color scales. Table 5 lists the most likely

Table 4
Spectral Results from the *Swift* XRT

Observation:	S-I	S-II	S-III	S-IV	S-V	S-VI	S-VII	S-VIII	S-IX
$F_{2-10\text{ keV}}$ [10^{-9} erg cm^{-2} s^{-1}]	1.15 ± 0.20	1.53 ± 0.12	2.27 ± 0.15	2.29 ± 0.11	3.69 ± 0.15	2.81 ± 0.12	1.91 ± 0.09	1.35 ± 0.20	1.16 ± 0.12
$N_{\text{H,1}}$ [10^{22} cm^{-2}]	63.6 ± 5.8	76.5 ± 12.3	49.1 ± 2.9	67.6 ± 8.0	49.4 ± 3.1	32.8 ± 1.4	39.3 ± 2.0	42.4 ± 5.2	61.6 ± 19.3
$N_{\text{H,2}}$ [10^{22} cm^{-2}]	0.0	21.1 ± 10.1	0.0	16.3 ± 9.8	0.0	0.0	0.0	0.0	19.8 ± 9.4
Cov. Frac.	1.0	0.945 ± 0.045	1.0	0.970 ± 0.031	0.988 ± 0.002	1.0	1.0	1.0	0.858 ± 0.134
PL_{Norm} [cm^{-2} s^{-1} keV^{-1}]	0.32 ± 0.17	0.80 ± 0.41	0.23 ± 0.07	0.84 ± 0.34	0.33 ± 0.09	0.46 ± 0.09	0.25 ± 0.06	0.12 ± 0.07	0.38 ± 0.25
PL_{r}	1.91 ± 0.36	1.33 ± 0.22	1.09 ± 0.24	1.19 ± 0.17	0.61 ± 0.12	1.01 ± 0.09	0.85 ± 0.12	0.67 ± 0.26	1.23 ± 0.27
Fe $K\alpha$ A [10^{-3} s^{-1} cm^{-2}]	9.9 ± 2.4	5.0 ± 1.8	12.2 ± 3.6	7.6 ± 2.0	18.6 ± 3.4	8.9 ± 2.8	8.9 ± 1.4	9.5 ± 6.4	3.8 ± 1.1
Fe $K\alpha$ E [keV]	6.56 ± 0.07	6.34 ± 0.05	6.37 ± 0.05	6.49 ± 0.04	6.52 ± 0.05	6.47 ± 0.04	6.43 ± 0.03	6.33 ± 0.06	6.33 ± 0.06
Fe $K\alpha$ σ [keV]	0.317 ± 0.082	0.144 ± 0.085	0.316 ± 0.070	0.127 ± 0.073	0.296 ± 0.061	0.203 ± 0.058	0.145 ± 0.048	0.301 ± 0.078	0.200
χ^2/NDF	1.58	1.53	1.07	0.90	1.28	1.13	0.75	0.66	1.20

Note. The errors are on 1σ confidence level.

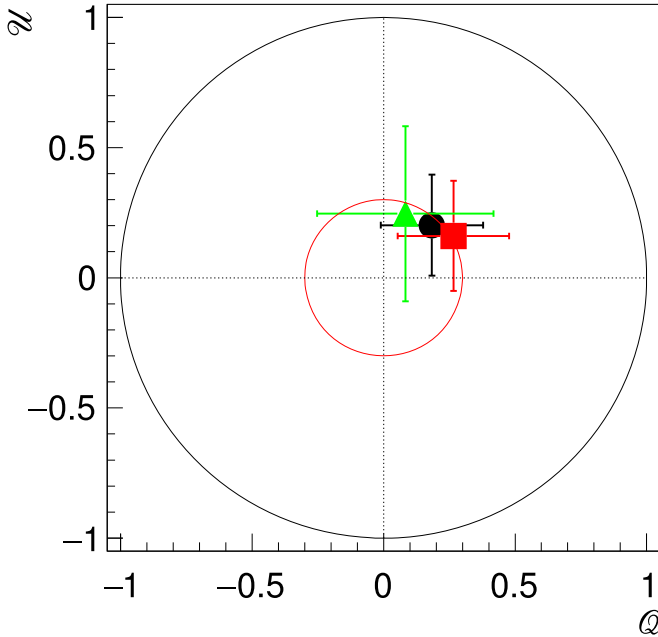


Figure 16. *X-Calibur* constraints on the linear polarization of the 15–35 keV GX 301–2 emission in the plane of the normalized Stokes parameters for the entire data set (black filled circle), the main pulse (red square, phase 0.8–1.14), and the bridge and secondary pulse (green triangle, phase 0.14–0.8) with 1σ statistical errors. Polarization fractions of 0%, 30% (for illustrative purposes), and 100% correspond to $Q = U = 0$ point at the center of the graph, the red circle, and the black circle, respectively.

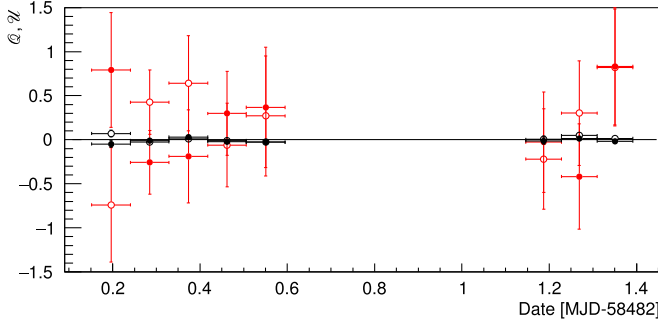


Figure 17. Q (filled circles) and U (open circles) parameters for the background-subtracted ON data (red) and the OFF data (black) as a function of time.

values of p_0 and ψ_0 together with the confidence intervals derived from the distributions in Figure 18. The table includes the 90% confidence interval upper limits on the polarization fraction p_0 calculated by marginalizing the probability density function $P(p_0, \psi_0)$ over ψ_0 .

6. Summary and Outlook

This paper presents the results of the observations of the accretion-powered X-ray pulsar GX 301–2 with *X-Calibur*, *NICER*, the *Swift* XRT and BAT, and *Fermi* GBM. The observations reveal a rare flaring period between the periastron flares associated with a spin up of the pulsar similar to earlier events (Bildsten et al. 1997; Koh et al. 1997). Historically, the spin of GX 301–2 exhibited values around 1.4 mHz (pulsar period: 715 s) between 1975 and 1985 and values around the current value of 1.47 mHz (pulsar period: 680 s) between 1993 and now (White et al. 1976; Nagase 1989; Lutovinov et al. 1994;

Bildsten et al. 1997; Koh et al. 1997), indicating an approximate equilibrium between spin-up and spin-down torques during these two long epochs (Lipunov 1992; Doroshenko et al. 2010). The spin-up epochs typically last about one orbit, in which the pulsar frequency changes linearly. The spin-up period, starting at the time of the *X-Calibur* observations, lasted for two orbits with a marked decline of the spin-up rate after the first orbit. The spin-up events start briefly after periastron (Figure 7 in this paper, and Figure 11 of Koh et al. 1997).

A possible interpretation of these signatures is that the neutron star acquires a temporary accretion disk (Koh et al. 1997) shortly after periastron passage. The temporary disk provides fuel for one orbit during which the pulsar spins up continuously, and is destroyed during the next periastron passage. The disk may form, for example, when the neutron star crosses the plasma stream from Wray 977 at the orbital phase of ~ 0.25 (Leahy & Kostka 2008). We note that during the spin-up periods, the crossing always results in a large increase in X-ray flux at the orbital phase of ≈ 0.4 . Independent of what exactly triggers the X-ray flares, it is an open question why only some flares spin up the neutron star.

We report here on the first constraints on the hard X-ray polarization of an accreting neutron star at energies fairly close to the cyclotron line energy. Owing to the short balloon flight time, the *X-Calibur* observations did not yield a definitive polarization detection, but did offer constraints on the polarization fraction and the polarization angle plane. The results can be compared to the predictions from Mészáros et al. (1988). The authors find that the propagation of the radiation in the ordinary and extraordinary mode and the strongly mode-dependent scattering cross sections can lead to very high ($\sim 80\%$) polarization fractions for certain pulse phases close to the cyclotron resonant energy. Interestingly, they find that fan-beam models predict, rather robustly, a positive correlation of the peak intensity and the polarization fraction. In contrast, pencil-beam models predict the opposite: a minimum (maximum) of the polarization fraction during the peak (valley) of the pulsed emission.

The *X-Calibur* observations constrain the polarization fraction in the 15–35 keV band, somewhat below the centroids of the CRSFs at 35 and 50 keV. The calculations of Mészáros et al. (1988) were carried out for a cyclotron resonance at 35 keV. At 25 keV the pencil-beam (fan-beam) model predicts polarization fractions of $\sim 20\%$ ($< 5\%$). The *X-Calibur* GX 301–2 result of $p_r = 27^{+38}_{-27}\%$ cannot distinguish between the two models. Doing so with high statistical certainty will require future observations with a one-sigma error of $< 4\%$.

Driven by this requirement, we are now working on an *X-Calibur* follow-up mission called *XL-Calibur* (Q. Abarr et al. 2020b, in preparation) which promises hard X-ray polarimetric observations with one to two orders of magnitude improved signal-to-background ratio. The mission uses the 12 m focal length mirror fabricated for the Formation Flight Astronomical Survey Telescope (Tsunemi et al. 2014) which offers more than three times larger effective areas than the current mirror (Awaki et al. 2014; Matsumoto et al. 2018). We furthermore expect more than one order of magnitude lower background rates owing to the use of thinner (0.8 mm thick) CZT detectors, improved shielding, and flights closer to solar maximum rather than solar minimum (see Shaw et al. 2003; Potgieter 2008). Simulated *XL-Calibur* observations of GX 301–2 (Figure 19) show that the improved mission could clearly distinguish

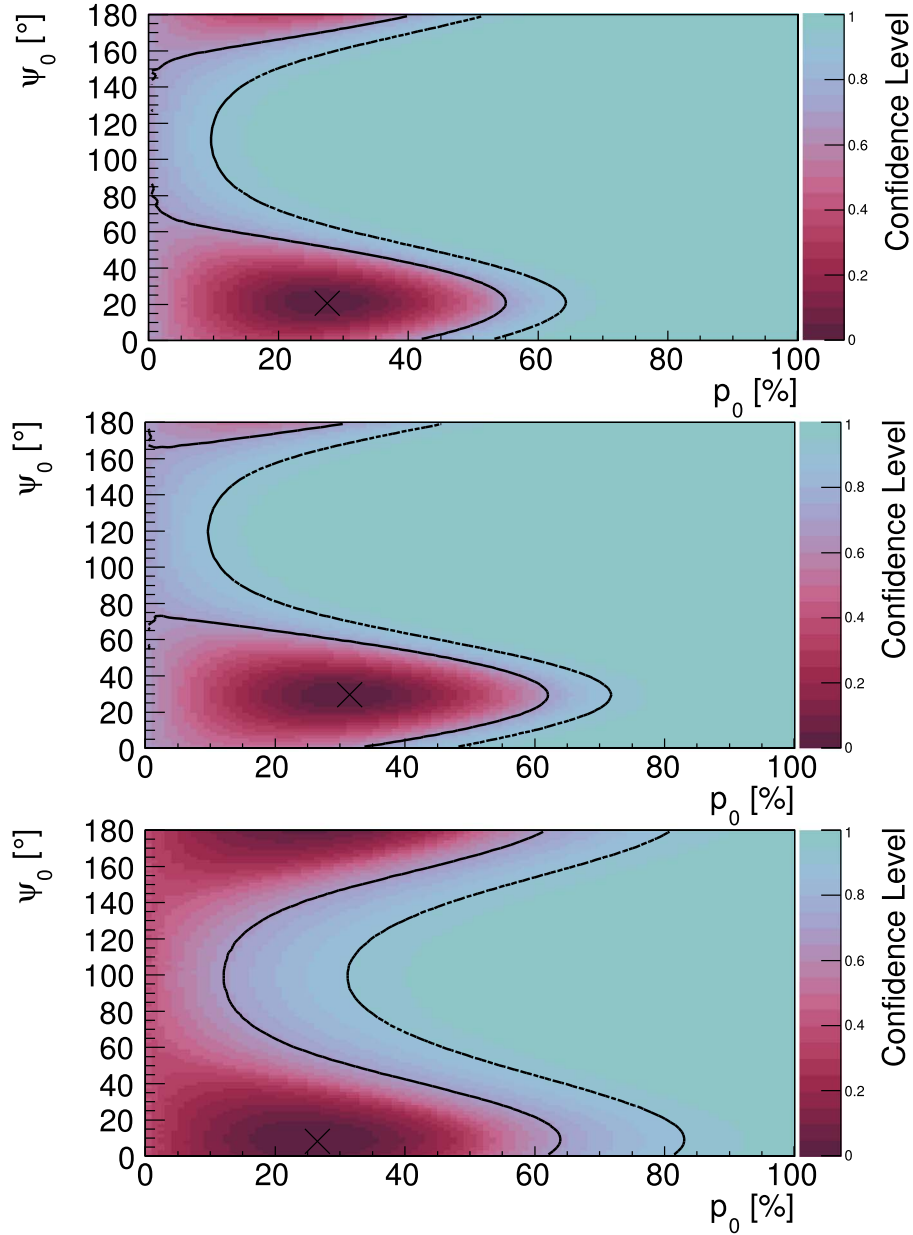


Figure 18. *X-Calibur* 15–35 keV polarization results in the polarization fraction, p_0 , and polarization angle, ψ_0 , plane for the entire emission (top), the main pulse (pulsar phase 0.8–1.14, center), and the bridge emission and the secondary pulse (pulsar phase 0.14–0.8, bottom). The most likely p_0 – ψ_0 combination is marked by a cross. The color scale shows the results for different confidence levels, and the contours delineate the 68.27% (1σ) and 90% confidence regions. The analysis only accounts for statistical errors.

Table 5
X-Calibur 15–35 keV Polarization Results

Phase Interval	Q [%]	U [%]	Deviation from $p = 0$ [σ]	p [%]	ψ [$^\circ$]	Upp. Lim. p (90% CL) [%]
All (0-1)	18.4 ± 19.4	20.2 ± 19.4	1.41	27^{+38}_{-27}	21 ± 43	46.9
Main Pulse (0.8–1.14)	26.6 ± 21.2	16.1 ± 21.1	1.47	32^{+41}_{-32}	30 ± 40	52.3
Bridge and Secondary Pulse (0.14–0.8)	8.3 ± 33.5	24.6 ± 33.6	0.78	27^{+55}_{-27}	10	62.2

Note. Errors on p and ψ are on 90% confidence level. The polarization angle of the third data set is unconstrained on the 90% confidence level.

between the fan-beam and the pencil-beam model. Joint observations with the *Imaging X-Ray Polarimetry Explorer* (2–8 keV, launching in 2021) (Weisskopf et al. 2016) and *XL-Calibur* (launching in 2022, 2023, and 2025), will enable detailed comparisons of predicted and observed signatures.

We thank A. Awaki (Ehime University), K. Hayashida (Osaka University, Project Research Center for Fundamental Sciences, ISAS), Y. Maeda (ISAS), H. Matsumoto (Osaka University, Project Research Center for Fundamental Sciences), T. Tamagawa (RIKEN), and K. Tamura (Nagoya University) for

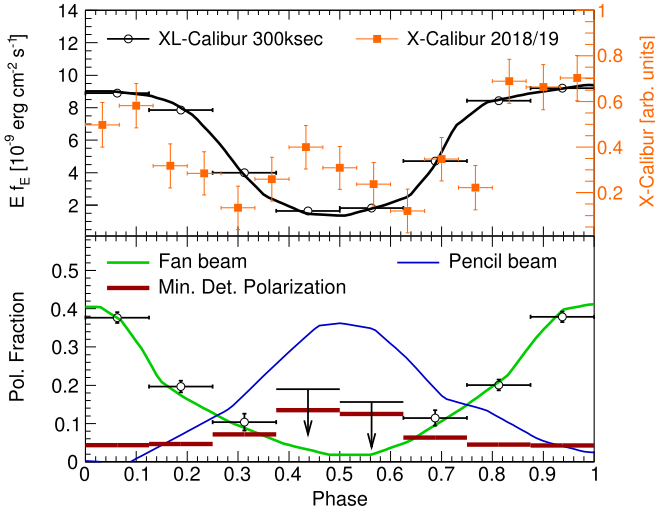


Figure 19. Simulated outcome of a 300 ks GX 301–2 observation with *XL-Calibur*, assuming a 20–50 keV flux of 700 mCrab, an energy spectrum similar to those from Fürst et al. (2018), and an atmospheric depth of 7 g cm^{-2} (equal to the mean depth of the 2018/2019 GX 301–2 observations). Top: assumed pulse profile (black line), measured *X-Calibur* 2018/19 pulse profile (orange data points), and simulated *XL-Calibur* results (black data points). Bottom: expected polarization fractions for the fan-beam (green line) and pencil-beam (blue line) models of Mészáros et al. (1988; model “45/45”). The black data points show the simulated *XL-Calibur* polarization fraction results for the fan-beam model, and the dark red lines show the Minimum Detectable Polarizations, i.e., the polarization fractions that *XL-Calibur* could detect with a 99% confidence level.

fruitful discussions and for their comments on this paper. We thank V. Mikhalev for contributing the code for barycentring the *X-Calibur* event times and Rakhee Kushwah (KTH, Oskar Klein Centre) for contributing to the flight monitoring shifts.

X-Calibur is funded by the NASA APRA program under contract number 80NSSC18K0264. We thank the McDonnell Center for the Space Sciences at Washington University in St. Louis for funding of an early polarimeter prototype, as well as for funds for the development of the ASIC readout. H.K. acknowledges NASA support under grants 80NSSC18K0264 and NNX16AC42G. KTH authors acknowledge support from the Swedish National Space Agency (grant No. 199/18). M.P. also acknowledges support from the Swedish Research Council (grant No. 2016-04929). H.K. acknowledges support from the National Science Foundation under the Independent Research and Development program.

Appendix A

Stokes Parameter Analysis of the *X-Calibur* Data

The analysis of the *X-Calibur* events starts with the de-rotation of the x and y coordinates of the energy deposition in the detector reference frame into the reference frame of the telescope truss. Subsequently, we correct for the offset of the focal spot of the X-ray mirror from the center of the scattering element as determined from the excess recorded in the rear CZT detector (Figure 9). Finally, the coordinates are referenced to the celestial north pole based on the truss orientation measured by the pointing system. Choosing a coordinate system with the y -coordinate pointing north and the x -coordinate pointing east, the azimuthal scattering angle

is given by:

$$\psi = \arctan(y/x), \quad (13)$$

so that $\psi = 0$ corresponds to scatterings along the north–south direction, and $0 < \psi < \pi/2$ corresponds to scatterings along the northeast direction. We calculate a set of Stokes parameters (Kislat et al. 2015) for the k th event:

$$i_k = 1 \quad (14)$$

$$q_k = -\frac{2}{\mu} \cos(2\psi_k) \quad (15)$$

$$u_k = -\frac{2}{\mu} \sin(2\psi_k). \quad (16)$$

The factor μ is the modulation factor (see Equation (3)). The minus signs in the expressions of q_k and u_k account for the 90° offset between the electric field vector of the photons and the preferred scattering direction. The factor $2/\mu$ normalizes q_k (u_k) so that its average is 1 for a beam 100% linearly polarized along the north–south direction (looking into the sky, 45° anti-clockwise from the north–south direction).

The k th event enters the analysis with weight w_k that is proportional to the expected signal-to-background ratio, and is the product of two functions (spectral analysis) or three functions (light curves) optimized with Monte Carlo simulations of the detector. The first function $f_1(z)$ depends on the position of the energy deposition along the optical axis (the z coordinate) and accounts for the approximately exponential distribution of the depths of the Compton scattering in the scattering element. As a consequence, most source photons are detected near the front of the polarimeter. The second function $f_2(x, y)$ depends on the position of the triggered pixel relative to the scattering element and is proportional to the azimuthal scattering angle $\Delta\psi$ that the pixel covers as seen from the axis of the scattering element. The function weighs events close to the middle of the side walls of the rectangular detector assembly more heavily than those close to the edges, as those pixels achieve a better signal-to-background ratio. The third function $f_3(E)$ (only for light curves) weighs events according to the energy E deposited in the CZT detectors and is proportional to the expected source detection rate as a function of energy accounting for the source spectrum, atmospheric absorption, and the mirror effective area.

With t_{ON} and t_{OFF} being the ON and OFF observation times and $\alpha = t_{\text{ON}}/t_{\text{OFF}}$, we define the total background-subtracted Stokes parameters as

$$I = \sum_{\text{ON}} w_k i_k - \alpha \sum_{\text{OFF}} w_k i_k, \quad (17)$$

$$Q = \sum_{\text{ON}} w_k q_k - \alpha \sum_{\text{OFF}} w_k q_k, \quad (18)$$

$$U = \sum_{\text{ON}} w_k u_k - \alpha \sum_{\text{OFF}} w_k u_k, \quad (19)$$

where the sums run over the ON and OFF events.

Compared to the unweighted analysis, the weighted analysis improves the signal-to-background ratio of the GX 301–2 results by $\sim 20\%$. Further sensitivity improvements might be achieved with a maximum likelihood analysis (see Krawczynski 2011; Lowell 2017; Lowell et al. 2017).

We calculate statistical errors on I , Q , U , and \mathcal{U} from error propagation. Each event contributes with the following rms

values to the analysis (Kislat et al. 2015):

$$\sigma_{i_k} = 1 \quad (20)$$

$$\sigma_{q_k} = \frac{\sqrt{2}}{\mu} \quad (21)$$

$$\sigma_{u_k} = \frac{\sqrt{2}}{\mu}. \quad (22)$$

The estimates of σ_{q_k} and σ_{u_k} are conservatively chosen for $p_0 = 0$. For $p_0 > 0$ the errors are smaller. When calculating the error on $Q(U)$, we assume that the errors on I and Q (I and U) are statistically independent. A toy simulation shows that this is indeed an excellent assumption.

Appendix B

Systematic Errors on the X-Calibur Polarization Results

We calibrated the polarimeter at the Cornell High Energy Synchrotron Source using a 40 keV beam with a $\sim 90\%$ polarization (Beilicke et al. 2014). The measurements were carried out with different polarimeter orientations allowing us to simulate an unpolarized beam by combining data taken at orientations differing by 90° . It is important to note that the rotation of the detector and shield assembly removes systematic errors due to detector non-uniformities (e.g., dead pixels, noisy pixels) and geometrical effects (including uncertainties in the distances between the center of the scattering element and the CZT detectors and gaps between the detectors). Based on the calibration data, we estimate that we know the modulation factor μ within an uncertainty of $\pm 2\%$. The uncertainty on μ introduces a relative systematic error on the measured polarization fraction p_r of $\Delta p_r = 2\% p_r$.

The misalignment of the center of the mirror point-spread function and the rotation axis of the polarimeter can lead to a spurious polarization that is independent of the true polarization fraction (Beilicke et al. 2014). Based on the image of GX 301–2 in the rear CZT detector (Figure 9), we estimate that the center of the point-spread function and the rotation axis of the polarimeter were offset by ($d = 1.5$ mm). Correcting for d , the uncertainty in d leads to a residual systematic polarization fraction error of $< 0.25\%$.

We performed the full Stokes analysis for the background data runs, and obtain Stokes parameters that are consistent with 0. For example, for the entire 15–35 keV background, we get

$$Q_{\text{OFF}} = -0.015 \pm 0.011 \quad (23)$$


$$U_{\text{OFF}} = 0.010 \pm 0.011, \quad (24)$$

where the errors are given for a 1σ confidence interval (see also Figure 17). The fact that the background looks unpolarized implies that an under- or over-subtraction of the background (owing for example to a time variable background) does not create a spurious polarization detection. We estimate that the background subtraction introduces a relative 5% error on measured polarization fractions.

Adding all systematic errors linearly, we get a total systematic error on the polarization fraction quoted in Equation (8).

ORCID iDs

B. Beheshtipour  <https://orcid.org/0000-0002-8524-1537>

N. Iyer  <https://orcid.org/0000-0001-6134-8105>

M. Kiss  <https://orcid.org/0000-0001-5191-9306>

H. Krawczynski  <https://orcid.org/0000-0002-1084-6507>

M. Pearce  <https://orcid.org/0000-0001-7011-7229>

C. Malacaria  <https://orcid.org/0000-0002-0380-0041>

C. Wilson-Hodge  <https://orcid.org/0000-0002-8585-0084>

References

- Adler, S. L. 1971, *AnPhy*, **67**, 599
- Adler, S. L., Bahcall, J. N., Callan, C. G., & Rosenbluth, M. N. 1970, *PRL*, **25**, 1061
- Arnaud, K. A. 1996, in ASP Conf. Ser. 101, *Astronomical Data Analysis Software and Systems V*, ed. G. Jacoby & J. Barnes (San Francisco, CA: ASP), 17
- Arnaud, K., Dorman, B., & Gordon, C. 2017, Xspec 12 (Greenbelt, MD: NASA), <https://heasarc.gsfc.nasa.gov/xanadu/xspec/>
- Arons, J., Klein, R. I., & Lea, S. M. 1987, *ApJ*, **312**, 666
- Awaki, H., Kunieda, H., Ishida, M., et al. 2014, *ApOpt*, **53**, 7664
- Barthelmy, S. D., Barbier, L. M., Cummings, J. R., et al. 2005, *SSRv*, **120**, 143
- Basko, M. M., & Sunyaev, R. A. 1975, *A&A*, **42**, 311
- Basko, M. M., & Sunyaev, R. A. 1976, *MNRAS*, **175**, 395
- Baumgartner, W. H., Tueller, J., Markwardt, C. B., et al. 2013, *ApJS*, **207**, 19
- Becker, P. A., Klochkov, D., Schönherr, G., et al. 2012, *A&A*, **544**, A123
- Becker, P. A., & Wolff, M. T. 2012, *ApJ*, **654**, 432
- Beilicke, M., Kislat, F., Zajczyk, A., et al. 2014, *JAI*, **3**, 1440008
- Beilicke, M., Kislat, F., Zajczyk, A., et al. 2015, in Proc. IEEE Aerospace Conf. (Piscataway, NJ: IEEE), doi:10.1109/AERO.2015.7118915
- Berendse, F., Owens, S. M., Serlemitsos, P. J., et al. 2003, *ApOpt*, **42**, 1856
- Bildsten, L., Chakrabarty, D., Chiu, J., et al. 1997, *ApJS*, **113**, 367
- Burnard, D., Arons, J., & Klein, R. 1991, *ApJ*, **367**, 575
- Burrows, D. N., Kennea, J. A., Abbey, A. F., et al. 2007, *Proc. SPIE*, **6686**, 668607
- Canuto, V., Lodenquai, J., & Ruderman, M. 1971, *PhRvD*, **3**, 2303
- Chanan, G. A., Novick, R., & Silver, E. H. 1979, *ApJL*, **228**, L71
- Clark, J. S., Najarro, F., Negueruela, I., et al. 2012, *A&A*, **541**, A145
- Davidson, K. 1973, *NPhS*, **246**, 1
- Doroshenko, V., Santangelo, A., Suleimanov, V., et al. 2010, *A&A*, **515**, A10
- Euler, H., & Kockel, B. 1935, *NW*, **23**, 246
- Farinelli, R., Ceccobello, C., Romano, P., & Titarchuk, L. 2012, *A&A*, **538**, A67
- Finger, M. H., Bildsten, L., Chakrabarty, D., et al. 1999, *ApJ*, **517**, 449
- Fürst, F., Falkner, S., Marcu-Cheatham, D., et al. 2018, *A&A*, **620A**, 153F
- Fürst, F., Suchy, S., Kreykenbohm, I., et al. 2011, *A&A*, **535**, A9
- Gaia Collaboration 2018, *yCat*, **1**, 345, 0
- Gendreau, K. C., Arzoumanian, Z., Adkins, P. W., et al. 2016, *Proc. SPIE*, **9905**, 99051H
- Gendreau, K. C., Arzoumanian, Z., & Okajima, T. 2012, *Proc. SPIE*, **8443E**, 13G
- Gnedin, Y. N. G. G., & Pavlov, G. G. 1974, *JETP*, **38**, 903
- Guo, Q., Beilicke, M., Garson, A., et al. 2013, *Aph*, **41**, 63
- Harding, A. K., & Lai, D. 2006, *RPPH*, **69**, 2631
- Heisenberg, W., & Euler, H. 1936, *ZPhy*, **98**, 714H
- Heyl, J., & Shaviv, N. J. 2000, *MNRAS*, **311**, 555
- Jenke, P. A., Finger, M. H., Wilson-Hodge, C. A., & Camero-Arranz, A. 2012, *ApJ*, **759**, 124
- Kalberla, P. M. W., Burton, W. B., Hartmann, D., et al. 2005, *A&A*, **440**, 775
- Kaper, L., van der Meer, A., & Najarro, F. 2006, *A&A*, **457**, 595
- Katsuta, J., Mizuno, T., Ogasaka, Y., et al. 2009, *NIMA*, **603**, 393
- Kii, T. 1987, *PASJ*, **39**, 781
- Kii, T., Hayakawa, S., Nagase, F., et al. 1986, *PASJ*, **38**, 751
- Kislat, F., Abarr, Q., Beheshtipour, B., et al. 2018, *JATIS*, **4**, 11004
- Kislat, F., Beheshtipour, B., Dowkontt, P., et al. 2017, *JAI*, **6**, 1740003
- Kislat, F., Clark, B., Beilicke, M., et al. 2015, *Aph*, **68**, 45
- Koh, D. T., Bildsten, L., Chakrabarty, D., et al. 1997, *ApJ*, **479**, 933
- Krawczynski, H. 2011, *Aph*, **34**, 784
- Krawczynski, H., Garson, A., Guo, Q., et al. 2011, *Aph*, **34**, 550
- Kreykenbohm, I., Wilms, J., Coburn, W., et al. 2004, *A&A*, **427**, 975
- Krimm, H. A., Holland, S. T., Corbet, R. H. D., et al. 2013, *ApJS*, **209**, 14
- Leahy, D. A., & Kostka, M. 2008, *MNRAS*, **384**, 747
- Lien, A., & Krimm, H. 2019, Swift/BAT Hard X-ray Transient Monitor (Greenbelt, MD: NASA), <https://swift.gsfc.nasa.gov/results/transients/>
- Lipunov, V. M. 1992, *Astrophysics of Neutron Stars* (New York: Springer)
- Liu, J., Soria, R., Qiao, E., & Liu, J. 2018, *MNRAS*, **480**, 4746

- Lowell, A. 2017, Polarimetric Studies of the Long Duration Gamma-Ray Burst GRB 160530A with the Compton Spectrometer and Imager (Berkeley, CA: UC Berkeley), <https://escholarship.org/uc/item/3b8664q5>
- Lowell, A. W., Boggs, S. E., Chiu, C. L., et al. 2017, *ApJ*, **848**, 120
- Lutovinov, A. A., Grebenev, S. A., Syunyaev, R. A., & Pavlinskii, M. N. 1994, *AstL*, **20**, 538
- Matsumoto, H., Awaki, H., Ishida, M., et al. 2018, *JATIS*, **4**, 011212
- Meegan, C., Lichti, G., Bhat, P. N., et al. 2009, *ApJ*, **702**, 791
- Mészáros, P. 1992, High-energy Radiation from Magnetized Neutron Stars, Theoretical Astrophysics (Chicago, IL: Univ. Chicago Press)
- Mészáros, P., Novick, R., Szentgyörgyi, A., Chanan, G. A., & Weisskopf, M. C. 1988, *ApJ*, **324**, 1056
- Mészáros, P., & Ventura, J. 1978, *PhRvL*, **41**, 1544
- Mushtukov, A. A., Suleimanov, V. F., Tsygankov, S. S., & Poutanen, J. 2015a, *MNRAS*, **447**, 1847
- Mushtukov, A. A., Suleimanov, V. F., Tsygankov, S. S., & Poutanen, J. 2015b, *MNRAS*, **454**, 2714
- Nabizadeh, A., Mönkkönen, J., Tsygankov, S. S., et al. 2019, *A&A*, **629**, 101
- Nagase, F. 1989, *PASJ*, **41**, 1
- Nelson, R., Salpeter, E., & Wassermann, I. 1993, *ApJ*, **418**, 874
- Ogasaka, Y., Tamura, K., Shibata, R., et al. 2008, *JaJAP*, **47**, 5743
- Oh, K., Koss, M., Markwardt, C. B., et al. 2018, *ApJS*, **235**, 4
- Okajima, T., Tamura, K., Ogasaka, Y., et al. 2002, *ApOpt*, **41**, 5417
- Parkes, G. E., Culhane, J. L., Mason, K. O., & Murdin, P. G. 1980, *MNRAS*, **191**, 547
- Postnov, K. A., Gornostaev, M. I., Klochkov, D., et al. 2015, *MNRAS*, **452**, 1601
- Potgieter, M. S. 2008, *JASTP*, **70**, 207
- Quinn, J. L. 2012, *A&A*, **538**, A65
- Sanchez Almeida, J., & Martinez Pillet, V. 1993, *ApOpt*, **32**, 4231
- Sato, N., Nagase, F., Kawai, N., et al. 1986, *ApJ*, **304**, 241
- Schönherr, G., Wilms, J., Kretschmar, P., et al. 2007, *A&A*, **472**, 353
- Schwinger, J. 1951, *PhRv*, **82**, 664
- Shaw, S. E., Westmore, M. J., Bird, A. J., et al. 2003, *A&A*, **398**, 391
- Staubert, R., Trümper, J., Kendziorra, E., et al. 2019, *A&A*, **622**, A61
- Strohmayer, T. E. 2017, *ApJ*, **838**, 72S
- Stuchlik, D. W. 2015, in Proc. AIAA AVIATION Forum (Dallas, TX: AIAA), doi:10.2514/6.2015-3039
- Suchy, S., Fürst, F., Pottschmidt, K., et al. 2012, *ApJ*, **745**, 124
- Toll, J. S. 1952, PhD thesis, Princeton Univ.
- Tsunemi, H., Nakajima, H., Anabuki, N., et al. 2014, *Proc. SPIE*, **9144**, 91442R
- Tueller, J., Krimm, H. A., Okajima, T., et al. 2005, *ExA*, **20**, 121
- Ventura, J. 1979, *PhRvD*, **19**, 1684
- Weisskopf, M. C., Ramsey, B., O'Dell, S., et al. 2016, *Proc. SPIE*, **9905**, 17
- Weisskopf, V. F. 1936, Kong. Dans. Vid. Selsk. Mat., **14**, 6
- West, B. F., Wolfram, K. D., & Becker, P. A. 2017, *ApJ*, **835**, 130
- White, N. E., Mason, K. O., Huckle, H. E., et al. 1976, *ApJL*, **209**, L119
- Wolff, M. T., Becker, P. A., Coley, J., et al. 2019, arXiv:1904.00108